This work was written as part of one of the author's official duties as an Employee of the United States Government and is therefore a work of the United States Government. In accordance with 17 U.S.C. 105, no copyright protection is available for such works under U.S. Law.

Public Domain Mark 1.0

https://creativecommons.org/publicdomain/mark/1.0/

Access to this work was provided by the University of Maryland, Baltimore County (UMBC) ScholarWorks@UMBC digital repository on the Maryland Shared Open Access (MD-SOAR) platform.

Please provide feedback

Please support the ScholarWorks@UMBC repository by emailing scholarworks-group@umbc.edu and telling us what having access to this work means to you and why it's important to you. Thank you.

AGU PUBLICATIONS

Geophysical Research Letters

RESEARCH LETTER

10.1002/2016GL071228

Key Points:
- Record Arctic warming focused in Barents and Kara Seas, southwestern Alaska, and central Arctic Ocean
- El Niño and teleconnections explain warming over land but not for the central Arctic
- Surface warming over the central Arctic consistent with the intrusion of enhanced water vapor and clouds

Supporting Information:
- Supporting Information S1

Correspondence to:
R. I. Cullather,
richard.cullather@nasa.gov

Citation:
Cullather, R. I., Y.-K. Lim, L. N. Boisvert, L. Brucker, J. N. Lee, and S. M. J. Nowicki (2016), Analysis of the warmest Arctic winter, 2015–2016, *Geophys. Res. Lett.*, *43*, 10,808–10,816, doi:10.1002/2016GL071228.

Received 16 SEP 2016
Accepted 5 OCT 2016
Accepted article online 6 OCT 2016
Published online 27 OCT 2016

©2016. American Geophysical Union. All Rights Reserved.

Analysis of the warmest Arctic winter, 2015–2016

Richard I. Cullather[1,2], Young-Kwon Lim[2,3], Linette N. Boisvert[1,4], Ludovic Brucker[4,5], Jae N. Lee[6,7], and Sophie M. J. Nowicki[4]

[1]Earth System Science Interdisciplinary Center, University of Maryland, College Park, Maryland, USA, [2]Global Modeling and Assimilation Office, National Aeronautics and Space Administration, Goddard Space Flight Center, Greenbelt, Maryland, USA, [3]I. M. Systems Group, Goddard Earth Sciences Technology and Research, College Park, Maryland, USA, [4]Cryospheric Science Laboratory, National Aeronautics and Space Administration, Goddard Space Flight Center, Greenbelt, Maryland, USA, [5]Universities Space Research Association, Goddard Earth Sciences Technology and Research, Columbia, Maryland, USA, [6]Joint Center for Earth Systems Technology, University of Maryland, Baltimore County, Baltimore, Maryland, USA, [7]Climate and Radiation Laboratory, National Aeronautics and Space Administration, Goddard Space Flight Center, Greenbelt, Maryland, USA

Abstract December through February 2015–2016 defines the warmest winter season over the Arctic in the observational record. Positive 2 m temperature anomalies were focused over regions of reduced sea ice cover in the Kara and Barents Seas and southwestern Alaska. A third region is found over the ice-covered central Arctic Ocean. The period is marked by a strong synoptic pattern which produced melting temperatures in close proximity to the North Pole in late December and anomalous high pressure near the Taymyr Peninsula. Atmospheric teleconnections from the Atlantic contributed to warming over Eurasian high-latitude land surfaces, and El Niño-related teleconnections explain warming over southwestern Alaska and British Columbia, while warm anomalies over the central Arctic are associated with physical processes including the presence of enhanced atmospheric water vapor and an increased downwelling longwave radiative flux. Preconditioning of sea ice conditions by warm temperatures affected the ensuing spring extent.

1. Introduction

There has been considerable attention on changing conditions in the summertime Arctic, where September sea ice extent has declined by 13.4% per decade over the satellite era [*Serreze et al*., 2016], and widespread, persistent surface melt has been observed on polar ice sheets [*Nghiem et al*., 2012; *Cullather et al*., 2016]. An important concept in the discussion of recent climate is the notion of polar amplification, in which surface air temperatures in high latitudes respond more strongly to anthropogenic forcing than the Earth as a whole [*Holland and Bitz*, 2003; *Serreze et al*., 2009; *Park et al*., 2015]. Polar amplification, as seen in prognostic climate simulations, is primarily concerned with the Arctic—due in part to the differing configuration of land surfaces in Northern and Southern Hemispheres [*Collins et al*., 2013]. It also exhibits a characteristic seasonal cycle that is a maximum in winter [*Manabe and Stouffer*, 1980; *Lu and Cai*, 2009; *Pithan and Mauritsen*, 2014]. While surface heating in summer serves to melt ice or is absorbed into the ocean, increasing temperatures in the Arctic winter season may influence atmospheric circulation or precondition the surface ice cover for earlier and enhanced melting during the ensuing summer [*Holland et al*., 2011; *Park et al*., 2015]. A warmer atmosphere also weakens the temperature gradient with the underlying ocean and thereby reduces sea ice growth. This alteration in the seasonal growth cycle may affect the ice cover over the ensuing weeks to months. In general, polar amplification is attributable to changes to the underlying cryospheric surface cover and its associated feedback [*Serreze and Barry*, 2011]. A thinning or loss of late summer sea ice cover reduces the insulation of the lower atmosphere from oceanic surface heat fluxes in subsequent winter months [*Screen and Simmonds*, 2010]. This also allows for the addition of water vapor into the lower troposphere [*Boisvert and Stroeve*, 2015; *Boisvert et al*., 2015], which may in turn affect surface radiative fluxes. Previous studies have also examined the relation between the Arctic winter climate and atmospheric teleconnections as a means of initiating anomalously warm conditions [e.g., *Dickson et al*., 2000; *Moritz et al*., 2002]. The observational record allows for exploring the relative roles of these processes during extreme events.

Long-term temperature reconstructions [*Hansen et al*., 2010] indicate that for the region of the north polar cap (70°N–90°N), the 2015–2016 Arctic winter temperature anomalies (December-January-February (DJF)) exceeded the previous warmest Arctic winter of 2011–2012 by more than 0.7°C and exceeded the warmest Arctic winter of the mid-Twentieth Century by more than 1.3°C. The temperature anomaly for the Arctic region

was also more than 3.5 times greater than that for the global average over the same period. The global average for the 3 month period was also the warmest in the time series extending back to 1880. The 2015–2016 winter has been reviewed by *Overland and Wang* [2016]. They relate the warm Arctic temperatures to anomalous circulation, which they characterize as a split of the tropospheric polar vortex. *Overland and Wang* [2016] assess potential contributions from the tropical Pacific on the anomalous circulation patterns. In this study, we describe the spatial patterns of temperature and other variables associated with this extraordinary period using a variety of remotely sensed observations and the Modern-Era Retrospective Analysis for Research and Applications version 2 (MERRA-2) atmospheric reanalyses [*Molod et al*., 2015; *Bosilovich et al*., 2016]. Reanalyses are susceptible to discontinuities from changes in observing systems but are useful due to observational scarcity and heterogeneity associated with available in situ records [*Lindsay et al*., 2014]. The relative roles of various mechanisms including a direct response to reduced sea ice cover, changes in atmospheric water vapor, and atmospheric teleconnection patterns are also explored.

2. Atmospheric Circulation and Sea Ice Cover

The spatial pattern of 2 m air temperature anomalies from atmospheric reanalysis for the three winter months (December 2015–February 2016; DJF) is shown in Figure 1a. Three foci of warm temperature anomalies are found in (1) the Barents Sea, (2) north of the Canadian Archipelago, and (3) the Bering Sea and southwestern Alaska. A few cold anomalies are also found over the Kamchatka Peninsula and south of Iceland in the North Atlantic [*Drijfhout et al*., 2012]. In the Barents Sea, anomalies for the DJF season in comparison to 1981–2010 baseline period exceed 10°C and are concentrated in the marginal sea ice zone near Svalbard, Franz Josef Land, and extending southeast to the Taymyr Peninsula. Figure 1a also indicates a close spatial correlation between these areas of positive temperature anomalies in the Barents and Kara Seas and negative anomalies in sea ice concentration [*Cavalieri et al*., 1996; *Maslanik and Stroeve*, 1999]. Sea ice concentration was lower than climatology by an average of about 20% in the Barents and Kara Seas, but larger anomalies are found locally. These anomalies correspond to an inhibition of winter ice growth, as well as an ice cover reduction by mechanical wind forcing. Figure 1a also indicates the poleward extent of the 0°C isotherm of maximum air temperature for the season, which reached close proximity to the North Pole. Over the period of 28–31 December 2015, a deep cyclonic system produced a strong advection of warm air and moisture through Fram Strait and into the Barents Sea and the central Arctic [*Boisvert et al*., 2016]. Warm temperature anomalies were then reinforced by a persistent region of low pressure in the North Atlantic during the month of January (see Figure S4b in the supporting information). January was also characterized by intense high pressure located near the Taymyr Peninsula (Figure S3k). Height anomalies for this location exceeded 300 geopotential meters at 500 hPa for January and are prominent in the 3 month averaged height anomalies shown in Figure 1b. The seasonal height patterns are broadly reflected in sea level pressure anomalies and in the integrated atmospheric moisture transport shown in Figure 1c, which indicates a strong poleward advection of water vapor from midlatitudes across the Barents Sea and into the central Arctic. Temperature anomalies shown over the Barents and Kara Seas and adjacent land areas are consistent with warm air advection along the western side of this height anomaly feature. In February, warm temperature anomalies continued in the vicinity of open water near Svalbard and Franz Josef Land, and were pervasive over the central Arctic Ocean—particularly in the Lincoln Sea and near the Canadian Archipelago. Positive geopotential height anomalies in February were also positioned over the central Arctic Ocean (see Figure S3l). The third center of warm temperature anomalies located over southwestern Alaska was initially present in December, but the magnitude increased substantially in January and February. Here surface air temperature anomalies exceeded 7°C for the 3 month period. As shown in Figure 1a, sea ice concentrations over the Bering Sea were also anomalously low by about 20% (see Text S2 in the supporting information for more details on sea ice concentration).

Negative sea ice concentration anomalies of large magnitude as shown for the Barents, Kara, and Bering Seas denote reductions in ice extent for these locations. Reduced sea ice concentration is also indicated along the eastern coast of Greenland. For the pan-Arctic region, the DJF sea ice extent was the lowest value in the satellite record (1979 to present), averaging 13.35×10^6 km^2 [*Fetterer et al*., 2002]. This compares with the 1980–2009 average extent of 14.39×10^6 km^2. Smaller reductions in ice concentration of less than 10% occurred along the northern coast of Alaska and in Baffin Bay. There were also slight increases in sea ice extent near cold temperature anomalies around the Kamchatka Peninsula.

19448007, 2016, 20, Downloaded from https://agupubs.onlinelibrary.wiley.com/doi/10.1002/2016GL071228, Wiley Online Library on [11/07/2023]. See the Terms and Conditions (https://onlinelibrary.wiley.com/terms-and-conditions) on Wiley Online Library for rules of use; OA articles are governed by the applicable Creative Commons License

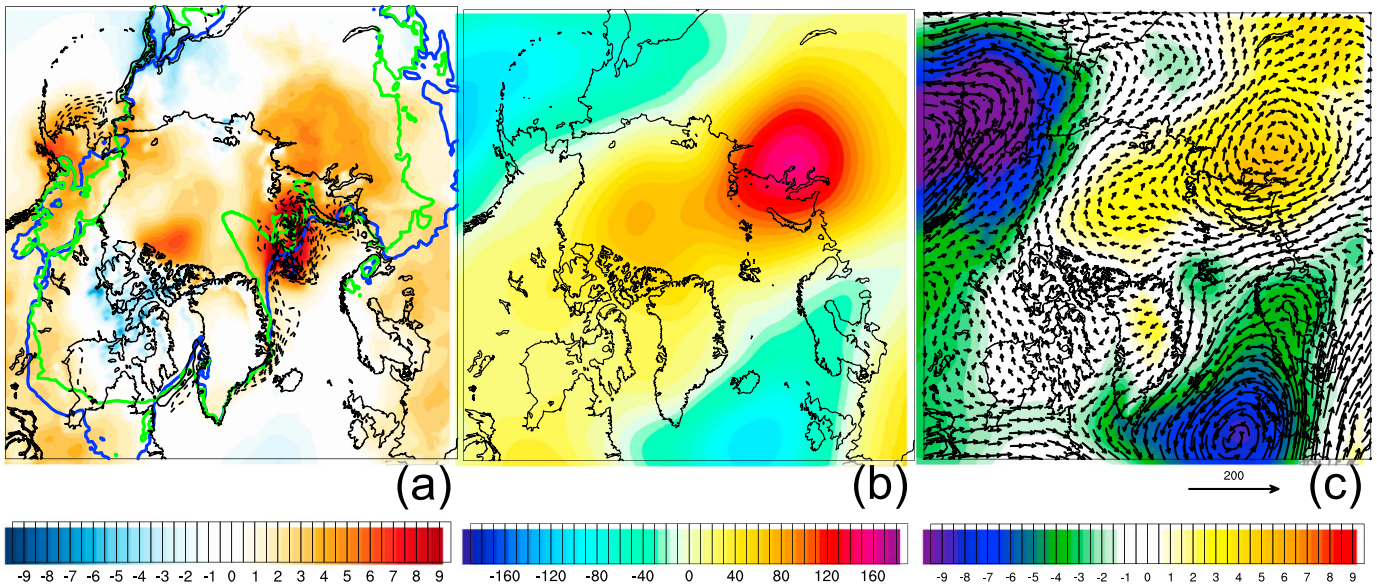

Figure 1. From MERRA-2 reanalysis [*Bosilovich et al.*, 2016] for poleward of 55°N: (a) the DJF 2015–2016 anomaly of 2 m air temperature, shaded every 0.5°C. The 0°C isotherm of the DJF maximum 2 m temperature determined from hourly values is indicated in green for 2015–2016 and in blue for the corresponding average over the base period of 1980–2009. The anomaly in sea ice fractional cover from passive microwave data [*Cavalieri et al.*, 1996; *Maslanik and Stroeve*, 1999] is contoured in black every 0.1 for the same time period, with dashed lines indicating negative values. Also from reanalysis, (b) the DJF 2015–2016 anomaly for 500 hPa geopotential height, shaded every 10 geopotential m. (c) The anomaly for sea level pressure for the same period, shaded every 0.5 hPa, with the anomaly of vertically integrated water vapor transport shown with vectors. The maximum vector is indicated as 200 kg m^{-1} s^{-1}.

3. Atmospheric Remote Sensing Observations

Anomalies in atmospheric conditions are further examined using the Atmospheric Infrared Sounder (AIRS) instrument on board the NASA EOS Aqua satellite, which makes multiple passes per day over the Arctic. The AIRS cross-track scanner provides a horizontal resolution of 13.5 km, which is then aggregated onto a 1°×1° grid [*Olsen*, 2011; *Parkinson*, 2003; *Susskind et al.*, 2014]. The AIRS baseline period of 2002 through 2015 is restricted by the length of time the instrument has been in orbit. For the Arctic, this period is thought to be substantially warmer than the 30 year baseline period used above to examine circulation and sea ice. Nevertheless, there is strong qualitative agreement in the spatial patterns of the reanalyses and AIRS temperatures. This is indicative of the large magnitude of anomalies for the 2015–2016 winter relative to even recent periods. MERRA-2 assimilates AIRS radiances, but this is restricted in the lower troposphere over snow and ice. Skin and air temperature, total precipitable water, downwelling longwave flux, and latent and sensible heat flux anomalies derived from AIRS data were further examined for this study. (Details on the AIRS retrievals and how the flux terms were calculated are located in Texts S3 and S4, respectively.) While these products are interrelated and may incur shared errors, they are produced sequentially [*Susskind et al.*, 2014].

Air temperature anomalies for the winter 2015–2016 from AIRS indicate a close spatial correlation with those of MERRA-2 shown in Figure 1a and are consistent with the unusual magnitude of warming found (see Figure S3). The period is found to be the warmest Arctic winter since AIRS launch in 2002. Surface skin temperature anomalies, based on the 13 year AIRS climatology (2002–2015), exceeded 8°C over the marginal sea ice zone near Barents Sea. The largest positive anomalies are found over the Barents and Kara Seas, with additional warm anomalies over the Eurasian continent as well as the northern part of North America, particularly over Alaska and the Bering Sea. A few cold anomaly locations are also found over the Kamchatka Peninsula and in the North Atlantic, similar to those seen in the reanalysis field.

Figure 2a shows the DJF 2015–2016 total precipitable water (column-integrated water vapor) anomaly field. Typically, seasonally averaged water vapor in the wintertime Arctic ranges from less than 2.5 kg m^{-2} over the central Arctic Ocean to greater than 8 kg m^{-2} in storm track regions of the western Barents Sea and in southwestern Alaska. Figure 2a indicates positive anomalies of greater than 1 kg m^{-2} as compared with the recent AIRS climatology for areas that are co-located with reduced sea ice cover over the Barents and Kara Seas and over the eastern Bering Sea. Positive anomalies are pervasive over most of the warm temperature anomaly

19448007, 2016, 20, Downloaded from https://agupubs.onlinelibrary.wiley.com/doi/10.1002/2016GL071228, Wiley Online Library on [11/07/2023]. See the Terms and Conditions (https://onlinelibrary.wiley.com/terms-and-conditions) on Wiley Online Library for rules of use; OA articles are governed by the applicable Creative Commons License

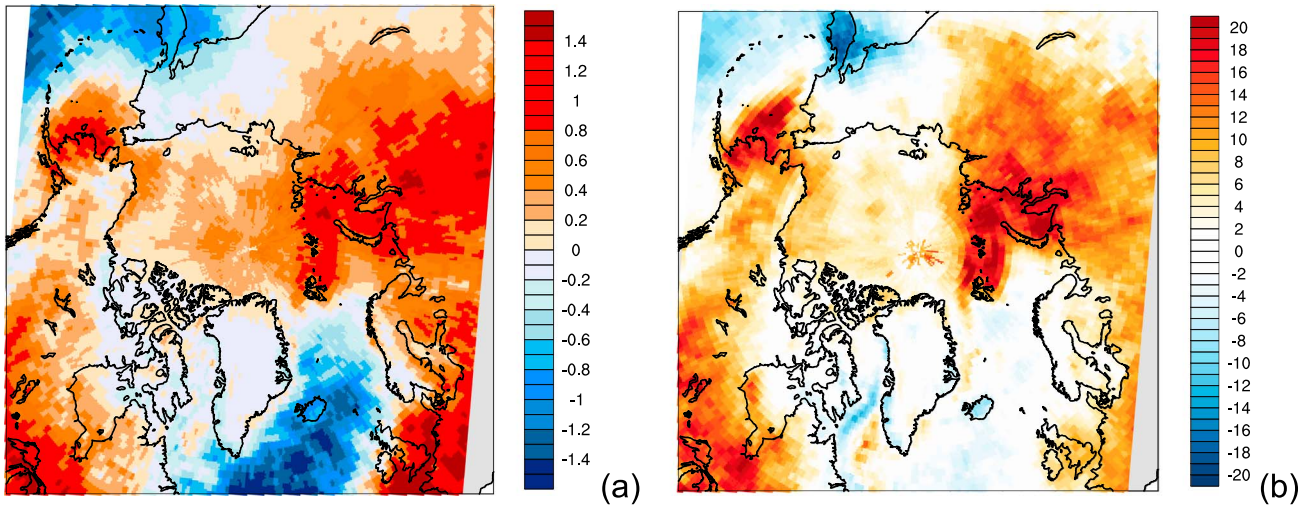

Figure 2. From AIRS data: the DJF 2015–2016 anomaly of (a) column precipitable water, shaded every 0.1 kg m^{-2}, and (b) surface downwelling longwave radiative flux, shaded every 1 W m^{-2}. The anomaly is computed for a base period of 2002–2015.

regions including the central Arctic and the Eurasian and North American land surfaces. Negative anomalies are present over the North Atlantic and North Pacific Oceans and eastern Siberia. By month, precipitable water anomalies followed a similar progression as surface air temperature anomalies, with primarily negative anomalies over most of the Arctic Ocean in December and large, positive anomalies in January and February. Particularly large positive anomaly magnitudes are found near Alaska and over the Barents and Kara Seas. In February, precipitable water anomalies became negative over Hudson Bay and the eastern areas of northern North America, while positive anomalies over the Kara and Barents Seas and adjacent land surfaces in northern Eurasia increased in magnitude. Precipitable water anomalies over the Kara Sea averaged 1 kg m^{-2} in January but were greater than 1.5 kg m^{-2} in February.

Figure 2b indicates surface downwelling longwave fluxes derived from AIRS data for DJF compared to climatology. Similar to the precipitable water anomalies, the downwelling longwave flux anomalies are positive over the entire pan-Arctic, with the largest anomalies of approximately 20 W m^{-2} that are found over the Barents, Kara, and Bering Seas. Positive anomalies of about 4 W m^{-2} are found over the central Arctic north of the Canadian Arctic Archipelago. The water vapor and downwelling longwave flux anomalies shown in Figures 2a and 2b are both derived from the AIRS instrument. However, similarities in the patterns suggest that the increased column water vapor is providing an enhanced downwelling thermal radiative flux to these locations of reduced ice cover. Over the third location of enhanced warmth in the central Arctic, water vapor and longwave flux anomalies are positive but small in magnitude.

Figure 3a shows the average cloud fraction for DJF 2015–2016 from AIRS data. Areas with higher cloud fractions are associated with locations over open water and marginal ice zones, while smaller amounts are present over the central Arctic ice pack. Cloud fraction anomalies for the same time period are shown in Figure 3b. Positive anomalies of greater than 10% are present over areas of largest warming anomalies in the northern Barents, Kara, and Bering Seas. Positive anomalies are also present over the central Arctic and northern Eurasia. Over land, Figure 3 indicates increased cloud cover over Eurasia and negative anomalies over the Canadian Arctic Archipelago. The changes in the observed cloud cover for the 2015–2016 winter shown in Figure 3b are broadly consistent with anomalies in precipitable water and downwelling longwave flux anomalies shown in Figure 2. In the Arctic, increases in atmospheric moisture and cloudiness are known to provide enhanced surface warming in the autumn and winter, providing a positive feedback for Arctic sea ice reduction [*Wu and Lee*, 2012; *Woods and Caballero*, 2016; *Park et al.*, 2015].

4. Atmospheric Teleconnections

An examination of reanalyses over the satellite era (1980 to present) indicates that the magnitude of the dominant January blocking pattern located near the Taymyr Peninsula is unprecedented. However, some

19448007, 2016, 20, Downloaded from https://agupubs.onlinelibrary.wiley.com/doi/10.1002/2016GL071228, Wiley Online Library on [11/07/2023]. See the Terms and Conditions (https://onlinelibrary.wiley.com/terms-and-conditions) on Wiley Online Library for rules of use; OA articles are governed by the applicable Creative Commons License

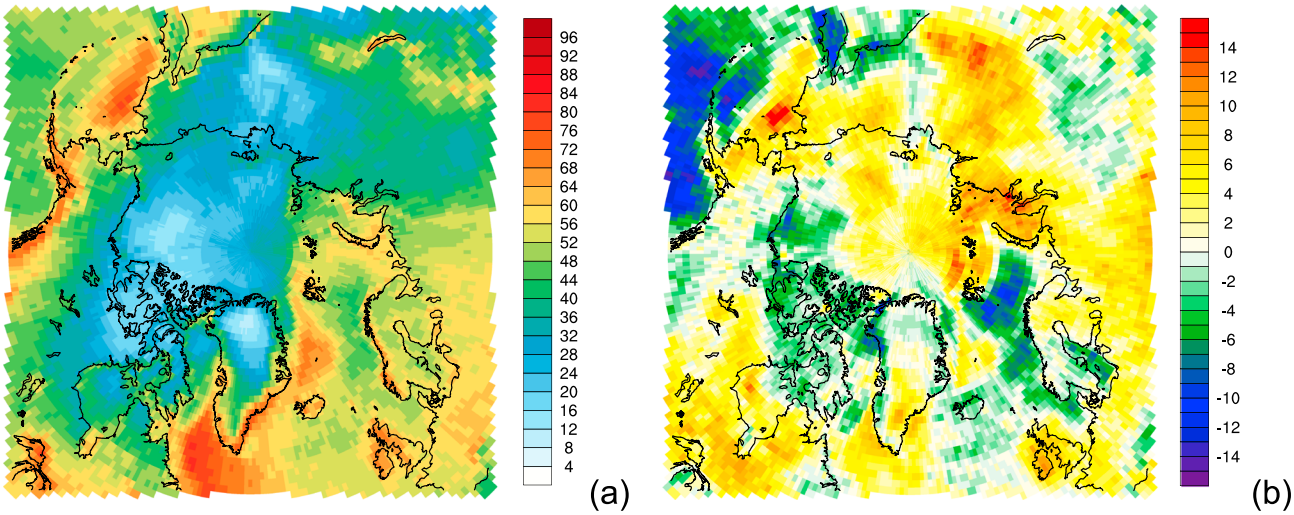

Figure 3. From AIRS data for DJF 2015–2016: (a) average cloud fraction, shaded every 4%, and (b) cloud cover anomaly, shaded every 1%. The anomaly is computed for a baseline period of 2002–2015.

aspects of the anomalous circulation are consistent with established teleconnection patterns of the atmosphere [e.g., *Wallace and Gutzler*, 1981; *Barnston and Livezey*, 1987]. Patterns that are known to play significant roles in middle- to high-latitude circulation variability include the North Atlantic Oscillation (NAO) [*Hurrell et al.*, 2003], the Pacific/North American (PNA) pattern [*L'Heureux et al.*, 2008], the East Atlantic-West Russia (EA/WR) pattern [*Lim*, 2015], the Scandinavian (SCA) pattern [*Bueh and Nakamura*, 2007], and the Tropical/Northern Hemisphere (TNH) pattern [*Mo and Livezey*, 1986]. These teleconnection patterns may be captured from empirical orthogonal function analysis of monthly 500 hPa geopotential height anomalies. Time series for each of these patterns were computed from reanalysis fields. The combined contribution of these modes was found to explain 40% of the observed variance. In Figure 4, 2 m temperature anomalies and 500 hPa height anomalies for the 2015–2016 winter are reconstructed by a linear combination of the monthly anomaly fields regressed onto the five teleconnection time series. These reconstructions are then compared with the actual anomaly fields. As seen in Figures 4a and 4b, the five dominant teleconnection patterns reproduce the anomalous warming over terrestrial land surfaces and in fact reproduce some of the warming over the Kara Sea. Coincident with the 2015–2016 winter was an intense El Niño–Southern Oscillation (ENSO) warm event, considered one of the strongest on record [*Klein*, 2015]. The PNA, a spatial pattern of alternating pressure anomalies extending over western North America, varies with its own internal variability [*Straus and Shukla*, 2002] but has also been related to tropical Pacific variability [*Younas and Tang*, 2013; *Philander*, 1983; *van Loon and Madden*, 1981]. The TNH pattern is also closely related to ENSO variability [*Zhang et al.*, 2016; *Mo and Livezey*, 1986]. Combined, the PNA and TNH modes explain 15% of the observed extratropical variance. As shown in Figure 4c, the combined contributions of these two modes produce warming over western North American high latitudes of up to 3°C for the winter season 2015–2016. The pattern of warming is consistent with *Cohen* [2016], who found that the ENSO influences on midlatitude weather are primarily found in the North Pacific/America sector with little relationship in the Atlantic/Eurasia sector. The combined contribution of the five teleconnection indices as shown in Figure 4b adequately represents winter temperature anomaly patterns over terrestrial land surfaces. While the overall patterns are similar, some differences may be found, particularly in the magnitude of the anomaly over southern Alaska. Critically, the teleconnections examined do not explain temperature anomalies over the central Arctic Ocean.

Also shown in Figures 4d–4f are reconstructed 500 hPa geopotential heights from teleconnection patterns as compared to the actual anomalies. As seen in Figure 4e, the teleconnection patterns remarkably capture the positive height anomalies over Eurasia. As shown in Figure 4f, the PNA and TNH patterns construct the negative height anomaly over the North Pacific Ocean and positive anomalies over northwestern North America associated with strong ENSO. The resulting southerly anomalous circulation over the northeastern Pacific produces significant warming over Alaska. Although the Pacific Decadal Oscillation (PDO) [*Mantua and Hare*, 2002] is not considered in this reconstruction, the positive phase of the PDO in 2015–2016 is suggested

19448007, 2016, 20, Downloaded from https://agupubs.onlinelibrary.wiley.com/doi/10.1002/2016GL071228, Wiley Online Library on [11/07/2023]. See the Terms and Conditions (https://onlinelibrary.wiley.com/terms-and-conditions) on Wiley Online Library for rules of use; OA articles are governed by the applicable Creative Commons License

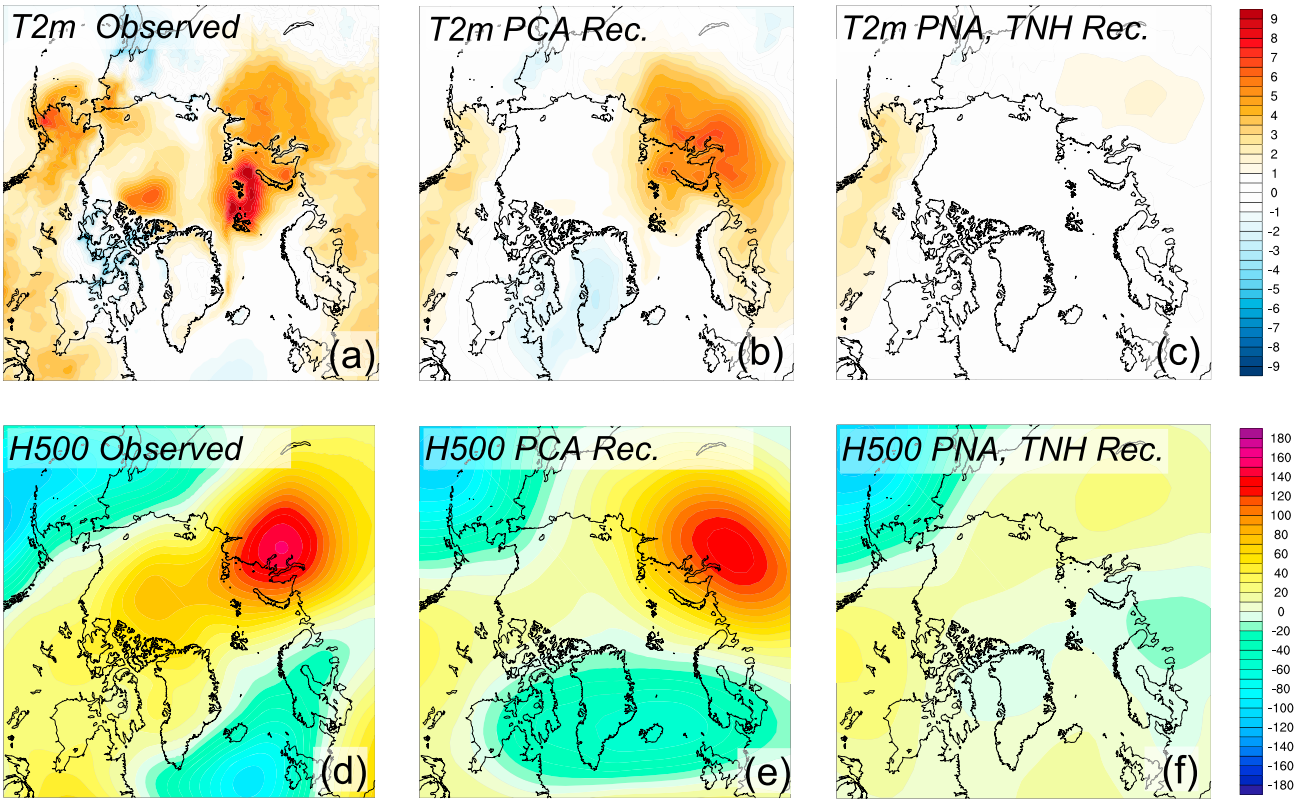

Figure 4. Reanalysis DJF 2015–2016 2 m temperature anomaly: (a) observed, (b) reconstructed from five principal components (see text), and (c) reconstructed from the Pacific/North America and Tropical/Northern Hemisphere principal components. Contours are shaded every 0.5°C. Reanalysis DJF 2015–2016 500 hPa geopotential height anomaly: (d) observed, (e) reconstructed from five principal components, and (f) reconstructed from the Pacific-North America and Tropical-North America principal components. Contours are shaded every 10 geopotential meters.

to be related to warming over this region, as the PDO is associated with southerly flow anomalies near Alaska [*Papineau*, 2001], similar to the PNA and TNH. Over Eurasia, the combined NAO, EA/WR, and SCA teleconnections resulted in positive height anomalies for 2015–2016 centered near the Taymyr Peninsula; however, the reconstructed height anomalies are of smaller magnitude than was actually experienced and do not extend into the central Arctic. The reconstructed Eurasian height anomaly shown in Figure 4e is about 20 m less than for the observed field and is more zonally oriented. The constructed height anomaly near 90°E nevertheless may provide favorable conditions for southerly flow to the west of the positive anomaly center, allowing for warm air advection over the northern Ural Mountains and adjacent Barents and Kara Seas.

5. Summary and Discussion

The influence of atmospheric teleconnections on the large-scale circulation generally explain anomalous warming patterns over the continents during the Arctic winter of 2015–2016. In particular, the teleconnections of the PNA and the TNH, known to be influenced by the intense ENSO warm event that occurred in this winter, explain warm temperature conditions over western North American high latitudes (southwestern Alaska and British Columbia). Additional teleconnections also broadly explain general warming patterns over Eurasia but do not address the magnitude of circulation and temperature anomalies and do not explain conditions over the central Arctic Ocean. The dynamic and/or thermodynamic inhibition of sea ice growth over Arctic marginal seas in the far North Atlantic provided additional sources of heat and moisture to the overlying atmosphere. These fluxes markedly altered the moisture and cloud content in close proximity to sea ice cover anomalies in the Barents and Kara Seas and provided a reinforcing feedback on surface warming via an anomalous downwelling longwave radiative flux. The additional, pervasive warming over the central Arctic Ocean that occurred in February is also associated with positive water vapor anomalies and enhanced

19448007, 2016, 20, Downloaded from https://agupubs.onlinelibrary.wiley.com/doi/10.1002/2016GL071228, Wiley Online Library on [11/07/2023]. See the Terms and Conditions (https://onlinelibrary.wiley.com/terms-and-conditions) on Wiley Online Library for rules of use; OA articles are governed by the applicable Creative Commons License

downwelling longwave radiation. Heat and moisture that entered the atmospheric column over anomalously open water in the Barents and Kara Seas or transported by synoptic activity from lower latitudes was further advected throughout the central Arctic by means of anomalous circulation. These results are consistent with *Overland and Wang* [2016].

An initial attribution analysis of Arctic conditions for 2015–2016 contrasts physical processes associated with reduced sea ice extent with teleconnection-induced circulation anomalies; however, the degree of interaction and feedback between these factors for this period requires further study. *Overland and Wang* [2016] characterized circulation patterns associated with the warming winter period as a split in the tropospheric polar vortex. Here we focus more closely on the unusual geopotential height anomalies over central Eurasia and the associated teleconnection patterns. In model experiments, the robust response of the atmosphere to sea ice reductions is associated with locally large upward turbulent heat fluxes but also with positive height anomalies over Arctic latitudes and troughing over the midlatitude North Atlantic [*Alexander et al*., 2004]. These conditions arise as open water fluxes influence overlying storm track patterns. The 2015–2016 winter circulation may be viewed as consistent with these patterns: a late December storm system inhibiting sea ice growth in North Atlantic marginal seas, followed by anomalous positive pressure to the north of the reduced ice cover. As sea ice cover is reduced in extent and thickness in a warming climate, it may become more mobile and thus more responsive to circulation patterns and their feedback, which may spatially alter, attenuate, or amplify teleconnection patterns in high latitudes. These factors may impact the agreement between the observed environment and those implied by teleconnection patterns, which are derived from historical conditions. A warming climate may also be more receptive to enhanced atmospheric water vapor, as has been observed in recent years [*Boisvert and Stroeve*, 2015], leading to enhanced feedback. In an anthropogenically warming climate, models have shown the largest atmospheric response occurs in winter and that heating provided by a seasonally ice-free Arctic Ocean is advected to terrestrial land areas over this season [*Deser et al*., 2010]. Thus, the 2015–2016 Arctic winter is relevant to understanding the potential larger-scale implications of a changing Arctic. Properties of winter and spring Arctic sea ice are predictive of ice cover conditions for the ensuing summer [*Guemas et al*., 2016; *Day et al*., 2014]. Arctic sea ice cover for spring 2016 remained at record low extent until mid-June [*Maslanik and Stroeve*, 1999]. Effects of the anomalous 2015–2016 Arctic winter may continue to be realized over the course of the following year.

Acknowledgments
Surface Temperature Analysis (GISTEMP) data were obtain from NASA Goddard Institute for Space Studies (http://data.giss.nasa.gov/gistemp/). Reanalysis fields [*Global Modeling and Assimilation Office*, 2015a, 2015b] and AIRS data products were obtained from the Goddard Earth Sciences Data and Information Services Center. Sea ice concentration data derived from passive microwave remote sensing with the NASA Team algorithm were obtained from the National Snow and Ice Data Center. Monthly indices were obtained from the NOAA Earth System Research Laboratory (http://www.esrl.noaa.gov/psd/data/climateindices/list/). The authors posthumously thank Andrew G. Slater for his helpful comments in review and thank one other anonymous reviewer. This study was funded by grants from the NASA Interdisciplinary Research in Earth Science (IDS) program to the first, fourth, and sixth authors.

References

Alexander, M. A., U. S. Bhatt, J. E. Walsh, M. S. Timlin, J. S. Miller, and J. D. Scott (2004), The atmospheric response to realistic Arctic sea ice anomalies in an AGCM during winter, *J. Clim.*, *17*(5), 890–905, doi:10.1175/1520-0442(2004)017<0890:TARTRA>2.0.CO;2.

Barnston, A. G., and R. E. Livezey (1987), Classification, seasonality and persistence of low-frequency atmospheric circulation patterns, *Mon. Weather Rev.*, *115*(6), 1083–1126, doi:10.1175/1520-0493(1987)115<1083:CSAPOL>2.0.CO;2.

Boisvert, L. N., and J. C. Stroeve (2015), The Arctic is becoming warmer and wetter as revealed by the Atmospheric Infrared Sounder, *Geophys. Res. Lett.*, *42*, 4439–446, doi:10.1002/2015GL063775.

Boisvert, L. N., D. L. Wu, T. Vihma, and J. Susskind (2015), Verification of air/surface humidity differences from AIRS and ERA-Interim in support of turbulent flux estimation in the Arctic, *J. Geophys. Res. Atmos.*, *120*, 945–963, doi:10.1002/2014JD021666.

Boisvert, L. N., A. A. Petty, and J. C. Stroeve (2016), The impact of the extreme winter 2015/2016 Arctic cyclone on the Barents-Kara seas, *Mon. Weather Rev.*, doi:10.1175/MWR-D-16-0234.1, in press.

Bosilovich, M. G., et al. (2016), MERRA-2. Initial evaluation of the climate, in *Global Modeling and Data Assimilation*, *Tech. Rep. Ser.*, vol. 43, edited by R. D. Koster NASA/TM-2015-104606, pp. 139, Goddard Space Flight Center, Greenbelt, Md.

Bueh, C., and H. Nakamura (2007), Scandinavian pattern and its climatic impact, *Q. J. R. Meteorol. Soc.*, *133*(629), 2117–2131, doi:10.1002/qj.173.

Cavalieri, D. J., C. L. Parkinson, P. Gloersen, and H. J. Zwally (1996), *Sea Ice Concentrations from Nimbus-7 SMMR and DMSP SSM/I-SSMIS Passive Microwave Data*, version 1, NASA National Snow and Ice Data Center Distributed Active Archive Center, Boulder, Colo., doi:10.5067/8GQ8LZQVL0VL.

Cohen, J. (2016), An observational analysis: Tropical relative to Arctic influence on midlatitude weather in the era of Arctic amplification, *Geophys. Res. Lett.*, *43*, 5287–5294, doi:10.1002/2016GL069102.

Collins, M., et al. (2013), Long-term climate change. Projections, commitments and irreversibility, in *Climate Change 2013. The Physical Science Basis. Contribution of Working Group I to the Fifth Assessment Report of the Intergovernmental Panel on Climate Change*, edited by T. F. Stocker, et al., pp. 1029-1136, Cambridge Univ. Press, Cambridge, U. K., and New York, doi:10.1017/CBO9781107415324.024.

Cullather, R. I., S. M. J. Nowicki, B. Zhao, and L. S. Koenig (2016), A characterization of Greenland Ice Sheet surface melt and runoff in contemporary reanalyses and a regional climate model, *Front. Earth Sci.*, *4*, 10, doi:10.3389/feart.2016.00010.

Day, J. J., S. Tietsche, and E. Hawkins (2014), Pan-Arctic and regional sea ice predictability: Initialization month dependence, *J. Clim.*, *27*(12), 4371–4390, doi:10.1175/JCLI-D-13-00614.1.

Deser, C., R. Tomas, M. Alexander, and D. Lawrence (2010), The seasonal atmospheric response to projected Arctic sea ice loss in the late twenty-first century, *J. Clim.*, *23*(2), 333–351, doi:10.1175/2009JCLI3053.1.

Dickson, R. R., T. J. Osborn, J. W. Hurrell, J. Meincke, J. Blindheim, B. Adlandsvik, T. Vinje, G. Alekseev, and W. Maslowski (2000), The Arctic Ocean response to the North Atlantic Oscillation, *J. Clim.*, *13*(15), 2671–2696, doi:10.1175/1520-0442(2000)013<2671:TAORTT>2.0.CO;2.

19448007, 2016, 20, Downloaded from https://agupubs.onlinelibrary.wiley.com/doi/10.1002/2016GL071228, Wiley Online Library on [11/07/2023]. See the Terms and Conditions (https://onlinelibrary.wiley.com/terms-and-conditions) on Wiley Online Library for rules of use; OA articles are governed by the applicable Creative Commons License

Drijfhout, S., G. J. van Oldenborgh, and A. Cimatoribus (2012), Is a decline of AMOC causing the warming hole above the North Atlantic in observed and modeled warming patterns?, *J. Clim.*, *25*(24), 8373–8379, doi:10.1175/JCLI-D-12-00490.1.

Fetterer, F., K. Knowles, W. Meier, and M. Savoie (2002), *Sea Ice Index*, Natl. Snow and Ice Data Cent., Boulder, Colo., doi:10.7265/N5QJ7F7W.

Global Modeling and Assimilation Office (GMAO) (2015a), MERRA-2 tavgM_2d_slv_Nx: 2d, Monthly mean, Time-Averaged, Single-Level, Assimilation, Single-Level Diagnostics, version 5.12.4, Goddard Space Flight Center Distributed Active Archive Center (GSFC DAAC), Greenbelt, Md., Accessed Mar 2016. doi:10.5067/AP1B0BA5PD2K.

Global Modeling and Assimilation Office (GMAO) (2015b), MERRA-2 tavgM_2d_int_Nx: 2d, Monthly mean, Time-Averaged, Single-Level, Assimilation, Vertically Integrated Diagnostics, version 5.12.4, Goddard Space Flight Center Distributed Active Archive Center (GSFC DAAC), Greenbelt, Md., Accessed Mar 2016. doi:10.5067/FQPTQ4OJ22TL.

Guemas, V., et al. (2016), A review on Arctic sea-ice predictability and prediction on seasonal to decadal time-scales, *Q. J. R. Meteorol. Soc.*, *142*(695), 546–561, doi:10.1002/qj.2401.

Hansen, J., R. Ruedy, M. Sato, and K. Lo (2010), Global surface temperature change, *Rev. Geophys.*, *48*, RG4004, doi:10.1029/2010RG000345.

Holland, M. M., and C. M. Bitz (2003), Polar amplification of climate change in coupled models, *Clim. Dyn.*, *21*(3), 221–232, doi:10.1007/s00382-003-0332-6.

Holland, M. M., D. A. Bailey, and S. Vavrus (2011), Inherent sea ice predictability in the rapidly changing Arctic environment of the Community Climate System Model, version 3, *Clim. Dyn.*, *36*(7), 1239–1253, doi:10.1007/s00382-010-0792-4.

Hurrell, J. W., Y. Kushnir, G. Ottersen, and M. Visbeck (2003), An overview of the North Atlantic Oscillation, in *The North Atlantic Oscillation. Climatic Significance and Environmental Impact*, edited by J. W. Hurrell et al., AGU, Washington, D. C., doi:10.1029/134GM01.

Klein, K. (2015), NOAA predicts strong El Niño, *Eos Trans. AGU*, *96*, doi:10.1029/2015EO035535.

L'Heureux, M. L., A. Kumar, G. D. Bell, M. S. Halpert, and R. W. Higgins (2008), Role of the Pacific-North American (PNA) pattern in the 2007 Arctic sea ice decline, *Geophys. Res. Lett.*, *35*, L20701, doi:10.1029/2008GL035205.

Lim, Y.-K. (2015), The East Atlantic/West Russia (EA/WR) teleconnection in the North Atlantic: Climate impact and relation to Rossby wave propagation, *Clim. Dyn.*, *44*(11), 3211–3222, doi:10.1007/s00382-014-2381-4.

Lindsay, R., M. Wensnahan, A. Schweiger, and J. Zhang (2014), Evaluation of seven different atmospheric reanalysis products in the Arctic, *J. Clim.*, *27*(7), 2588–2606, doi:10.1175/JCLI-D-13-00014.1.

Lu, J., and M. Cai (2009), Seasonality of polar surface warming amplification in climate simulations, *Geophys. Res. Lett.*, *36*, L16704, doi:10.1029/2009GL040133.

Manabe, S., and R. J. Stouffer (1980), Sensitivity of a global climate model to an increase of CO_2 concentration in the atmosphere, *J. Geophys. Res.*, *85*(C10), 5529–5554, doi:10.1029/JC085iC10p05529.

Mantua, N. J., and S. R. Hare (2002), The Pacific Decadal Oscillation, *J. Oceanogr.*, *58*(1), 35–44, doi:10.1023/A:1015820616384.

Maslanik, J., and J. Stroeve (1999), *Near-Real-time DMSP SSMIS Daily Polar Gridded Sea Ice Concentrations*, version 1, NASA National Snow and Ice Data Center Distributed Active Archive Center, Boulder, Colo., doi:10.5067/U8C09DWVX9LM.

Mo, K. C., and R. E. Livezey (1986), Tropical-extratropical geopotential height teleconnections during the Northern Hemisphere winter, *Mon. Weather Rev.*, *14*(12), 2488–2515, doi:10.1175/1520-0493(1986)114<2488:TEGHTD>2.0.CO;2.

Molod, A., L. Takacs, M. Suarez, and J. Bacmeister (2015), Development of the GEOS-5 atmospheric general circulation model. Evolution from MERRA to MERRA2, *Geosci. Model Dev.*, *8*(5), 1339–1356, doi:10.5194/gmd-8-1339-2015.

Moritz, R. E., C. M. Bitz, and E. J. Steig (2002), Dynamics of recent climate change in the Arctic, *Science*, *297*(5586), 1497–1502, doi:10.1126/science.1076522.

Nghiem, S. V., D. K. Hall, T. L. Mote, M. Tedesco, M. R. Albert, K. Keegan, C. A. Shuman, N. E. DiGirolamo, and G. Neumann (2012), The extreme melt across the Greenland Ice Sheet in 2012, *Geophys. Res. Lett.*, *39*, L20502, doi:10.1029/2012GL053611.

Olsen, E. T. (Ed) (2011), *AIRS/AMSU/HSB Version 5 Level 2 Product Levels, Layers and Trapezoids, Rep*, Jet Propul. Lab., Pasadena, Calif.

Overland, J. E., and M. Wang (2016), Recent extreme Arctic temperatures are due to a split polar vortex, *J. Clim.*, *29*(15), 5609–5616, doi:10.1175/JCLI-D-16-0320.1.

Papineau, J. M. (2001), Wintertime temperature anomalies in Alaska correlated with ENSO and PDO, *Int. J. Climatol.*, *21*(13), 1577–1592, doi:10.1002/joc.686.

Park, H.-S., S. Lee, S. W. Son, S. B. Feldstein, and Y. Kosaka (2015), The impact of poleward moisture and sensible heat flux on Arctic winter sea ice variability, *J. Clim.*, *28*(13), 5030–5040, doi:10.1175/JCLI-D-15-0074.1.

Parkinson, C. L. (2003), Aqua: An Earth-observing satellite mission to examine water and other climate variables, *IEEE Trans. Geosci. Remote Sens.*, *41*(2), 173–183.

Philander, S. G. H. (1983), El Niño–Southern Oscillation phenomena, *Nature*, *302*(5906), 295–301, doi:10.1038/302295a0.

Pithan, F., and T. Mauritsen (2014), Arctic amplification dominated by temperature feedbacks in contemporary climate models, *Nat. Geosci.*, *7*(3), 181–184, doi:10.1038/ngeo2071.

Screen, J. A., and I. Simmonds (2010), The central role of diminishing sea ice in recent Arctic temperature amplification, *Nature*, *464*(7293), 1334–1337, doi:10.1038/nature09051.

Serreze, M. C., and R. G. Barry (2011), Processes and impacts of Arctic amplification. A research synthesis, *Global Planet. Change*, *77*(1-2), 85–96, doi:10.1016/j.gloplacha.2011.03.004.

Serreze, M. C., A. P. Barrett, J. C. Stroeve, D. N. Kindig, and M. M. Holland (2009), The emergence of surface-based Arctic amplification, *Cryosphere*, *3*(1), 11–19, doi:10.5194/tc-3-11-2009.

Serreze, M. C., J. Stroeve, A. P. Barrett, and L. N. Boisvert (2016), Summer atmospheric circulation anomalies over the Arctic Ocean and their influences on September sea ice extent. A cautionary tale, *J. Geophys. Res. Atmos.*, *121*, doi:10.1102/2016JD025161.

Straus, D. M., and J. Shukla (2002), Does ENSO force the PNA?, *J. Clim.*, *15*(17), 2340–2358, doi:10.1175/1520-0442(2002)015<2340:DEFTP>2.0.CO;2.

Susskind, J., J. M. Blaisdell, and L. Iredell (2014), Improved methodology for surface and atmospheric soundings, error estimates, and quality control procedures: The atmospheric infrared sounder science team version-6 retrieval algorithm, *J. Appl. Remote Sens.*, *8*(1), 084994, doi:10.1117/1.JRS.8.084994.

van Loon, H., and R. A. Madden (1981), The Southern Oscillation. Part I. Global associations with pressure and temperature in northern winter, *Mon. Weather Rev.*, *109*(6), 1150–1162, doi:10.1175/1520-0493(1981)109<1150:TSOPIG>2.0.CO;2.

Wallace, J. M., and D. S. Gutzler (1981), Teleconnections in the geopotential height field during the Northern Hemisphere winter, *Mon. Weather Rev.*, *109*(4), 784–812, doi:10.1175/1520-0493(1981)109<0784:TITGHF>2.0.CO;2.

Woods, C., and R. Caballero (2016), The role of moist intrusions in winter Arctic warming and sea ice decline, *J. Clim.*, doi:10.1175/JCLI-D-15-0773.1, in press.

19448007, 2016, 20, Downloaded from https://agupubs.onlinelibrary.wiley.com/doi/10.1002/2016GL071228, Wiley Online Library on [11/07/2023]. See the Terms and Conditions (https://onlinelibrary.wiley.com/terms-and-conditions) on Wiley Online Library for rules of use; OA articles are governed by the applicable Creative Commons License

Wu, D. L., and J. N. Lee (2012), Arctic low cloud changes as observed by MISR and CALIOP: Implication for the enhanced autumnal warming and sea ice loss, *J. Geophys. Res.*, *117*, D07107, doi:10.1029/2011JD017050.

Younas, W., and Y. Tang (2013), PNA predictability at various time scales, *J. Clim.*, *26*(22), 9090–9114, doi:10.1175/JCLI-D-12-00609.1.

Zhang, T., M. P. Hoerling, J. Perlwitz, and T. Xu (2016), Forced atmospheric teleconnections during 1979-2014, *J. Clim.*, *29*(7), 2333–2357, doi:10.1175/JCLI-D-15-0226.1.

19448007, 2016, 20, Downloaded from https://agupubs.onlinelibrary.wiley.com/doi/10.1002/2016GL071228, Wiley Online Library on [11/07/2023]. See the Terms and Conditions (https://onlinelibrary.wiley.com/terms-and-conditions) on Wiley Online Library for rules of use; OA articles are governed by the applicable Creative Commons License